

Behavior-Inspired Neural Networks for Relational Inference

Yulong Yang*
Naomi Leonard

Bowen Feng*
Adji Busso Dieng
Princeton University

Keqin Wang
Christine Allen-Blanchette

Abstract

From pedestrians to Kuramoto oscillators, interactions between agents govern how a multitude of dynamical systems evolve in space and time. Discovering how these agents relate to each other can improve our understanding of the often complex dynamics that underlie these systems. Recent works learn to categorize relationships between agents based on observations of their physical behavior. These approaches are limited in that the relationship categories are modelled as outcomes of categorical distribution, when in real world systems categories often intermingle and interact. In this work, we introduce a level of abstraction between the observable behavior of agents and the latent categories that determine their behavior. To do this, we learn a mapping from agent behavior to agent preferences for each latent category in a graph neural network. We integrate the physical proximity of agents and their preferences in a nonlinear opinion dynamics model which provides a mechanism to identify mutually exclusive latent categories, predict an agent’s evolution in time, and control an agent’s physical behavior. We demonstrate the utility of our model for learning interpretable categories, and its efficacy on long-horizon prediction across several benchmarks where we outperform existing methods.

1 Introduction

Multi-agent systems are found in domains as diverse as astronomy [1, 2], biology [3, 4, 5], physics [6, 7], and

sports [8, 9]. Understanding how these systems evolve in time has the potential to provide insights useful for the discovery of unknown physics, the rules governing collective behavior, and engineering design. Predicting the evolution of complex systems is a fundamental challenge in the learning literature. Early black-box models determine future states from past states without regard for contextual information [10, 11]. More recent approaches improve upon these models by incorporating information about environmental conditions and the behavior of other agents [12, 13, 14, 15, 16]. While incorporating contextual information has led to more powerful trajectory prediction models, the opacity of these models limits our ability to leverage them to better understand the role of inter-agent relationships.

Recent work in relational inference attempts to address this limitation by explicitly modelling inter-agent relationships [17, 18, 19, 20, 21, 22]. Discovering inter-agent relationships is challenging, however, since ground truth labels are typically unavailable, and the relevant relationships may be unknown at design time. Graph neural network (GNN) based approaches such as [19, 20, 21, 22] model inter-agent relationship categories with a categorical variable. In their seminal work, the authors of [19] learn a latent representation of inter-agent relationships in a trajectory prediction pipeline. The authors of [20] improve on this approach by modeling inter-agent relationships as time varying and the authors of [21] improve model expressivity by representing node features as a hypergraph. While these methods are able to predict future observations of a number of systems, the underlying assumption that inter-agent relationships are determined by a single relationship category diverges from what we observe in the real world.

In contrast to these models, opinion dynamics models assume agents have preferences for multiple categories, and that these preferences evolve in time. The nonlinear opinion dynamics (NOD) model introduced in [23], has been used to model a variety of societal systems [24, 25, 26, 27, 28, 29, 30, 31]. The nonlinear nature of this model introduces a bifurcation which

* denotes equal contribution.
Preprint. Under review.

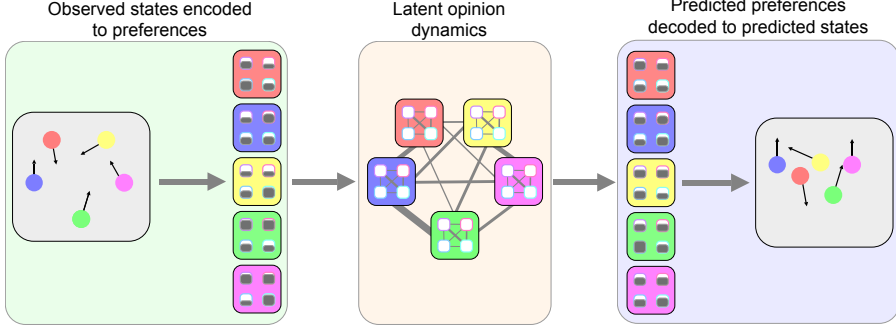


Figure 1: **Behavior-inspired neural network for relational inference.** BINNs allow for relational inference using inter-agent distance and a learned representation of inter-category interactions. The physical states of agents are encoded to preferences for a set of latent categories. Preferences are propagated forward in time using a nonlinear opinion dynamics model with learned parameters. Predicted preferences are then decoded to physical states as predicted future physical states.

allows preferences to quickly and flexibly respond to changes in environmental inputs. A limitation of this method, however, is that the relationship between agent preferences for a set of categories and their observable behavior must be known a priori.

In our model, *Behavior-inspired Neural Network* (BINN), we combine the flexibility of GNN models with the interpretability of nonlinear opinion dynamics for a new approach to relational inference. Concretely, our contributions are the following:

- In contrast to existing opinion dynamics models which require observability of agent preferences, we learn a representation of agent preferences from physical observations.
- In contrast to existing relational inference approaches which model relationship categories as a categorical variable, we use the NOD inductive bias to model the evolution of real-valued agent preferences on a set of latent categories.
- By incorporating the NOD inductive bias, we can identify mutually exclusive categories, predict an agent’s evolution in time, and control an agent’s behavior.

We demonstrate the utility of our approach for identifying mutually exclusive categories on multiple illustrative examples and demonstrate the efficacy of our approach for trajectory prediction tasks.

2 Related Work

Trajectory prediction. In contrast to traditional control approaches which tune a set of model parameters from all available trajectories (i.e., sequences of physical positions) [32, 33, 34, 35], early deep learning

approaches learn to map a sequence of input states to future states directly [11]. Later efforts incorporated external influences (e.g., behavior of other agents, environmental conditions) [12, 13, 14, 15, 16] and temporal dependencies [16, 36, 37, 38, 39], and recent work has used graph based methods to model multi-agent dynamics [40, 41]. While these methods are able to predict future system states, they do not predict which agents interact or how they interact, a limitation which motivates relational inference.

Relational inference. The goal of relational inference is to infer inter-agent relationships in a multi-agent system [17, 19, 20, 21, 22]. This task is challenging since, in general, the relationships between agents is unknown. Approaches to this challenge include: CommNet [17] which learns a continuous communication protocol for fully cooperative multi-agent tasks; Neural Relational Inference [19] which learns time invariant inter-agent relationships; Dynamic Neural Relational Inference [20] which learns time varying inter-agent relationships; GroupNet [21] which uses a multiscale hypergraph representation of the input for improved expressivity; and EquiMotion [22] which incorporates an equivariance constraint to ensure the dynamics transform predictably to Euclidean shifts of the input data. Our work differs from these approaches in our representation of relationship categories. Our categories exist in the space of agent preferences rather than the physical space, and our categories are flexible and interacting, rather than mutually exclusive and independent.

Consensus dynamics. In control and robotics, consensus dynamics [42] have been used in a myriad of settings to model the dynamics and control the behavior of multi-agent systems. In [43], the authors propose a linear model for prediction and control of multi-agent systems. In [44], the authors use a linear consensus

dynamics model for coordinated surveying with underwater gliders. In [45], the authors use the consensus dynamics framework to develop rectilinear and circular consensus control laws for multi-vehicles systems. In [46], the authors use consensus dynamics to improve data collection in a mobile sensor network. In [47], the authors use consensus dynamics to understand the robustness of starling flocking behavior. Even with this breadth of application, there are several draw backs to a linear model of opinion formation; specifically, the naive implementation results in dynamics that only yields consensus [48, 49] and the formation of opinions in response to inputs is slow.

Nonlinear opinion dynamics. The noted short comings of linear consensus dynamics models are resolved in the nonlinear opinion dynamics model proposed in [23]. As the model is nonlinear, the dynamics result in a bifurcation and opinions can evolve to dissensus quickly. Nonlinear opinion dynamics have been used to model a variety of systems. In [24, 25, 26, 27] nonlinear opinion dynamics model information spread in settings such as political polarisation. In [28], nonlinear opinion dynamics is used to resolve deadlock, and in [29], it is used for collision avoidance. In [30, 31], nonlinear opinion dynamics is used for task switching in robotic swarms in trash collecting robot teams. In contrast to these works, where the model has direct access agent opinions (i.e., preferences), we learn a mapping between physical states and agent preferences.

3 Background

Nonlinear dynamics differ from linear dynamics in that they are able to exhibit bifurcations [50, 51, 52]. Nonlinear opinion dynamics [53] leverage bifurcations for fast and flexible decision making even with weak input signals [23]. Our BINN model integrates a nonlinear opinion dynamics inductive bias to interpretably and flexibly model agent behavior.

3.1 Nonlinear opinion dynamics

Consider a multi-agent system of $\mathcal{N}_a \in \mathbb{N}$ agents, each possessing real-valued preferences about $\mathcal{N}_o \in \mathbb{N}$ categories. Each category represents a belief or desire (e.g., take a physical action, undertake a task), and an agent's preference for a category can be positive, neutral, or negative (the preference magnitude corresponds to preference strength). Changes to an agent's preference for a category depend on extrinsic and intrinsic parameters. Concretely, the changes to agent i 's preference for category j can be determined by the following nonlinear differential equation proposed in [23]

$$\begin{aligned} \dot{z}_{ij} = & -d_{ij}z_{ij} + \mathcal{S} \left(u_i \left(\alpha_{ij}z_{ij} + \sum_{\substack{k=1 \\ k \neq i}}^{\mathcal{N}_a} a_{ik}^a z_{kj} \right. \right. \\ & \left. \left. + \sum_{\substack{l=1 \\ l \neq j}}^{\mathcal{N}_o} a_{jl}^o z_{il} + \sum_{\substack{k=1 \\ k \neq i}}^{\mathcal{N}_a} \sum_{\substack{l=1 \\ l \neq j}}^{\mathcal{N}_o} a_{ik}^a a_{jl}^o z_{kl} \right) \right) + b_{ij}. \end{aligned} \quad (1)$$

The parameters $d_{ij} \geq 0$, $u_i \geq 0$, and $\alpha_{ij} \geq 0$ are intrinsic to the agent. The damping d_{ij} represents how resistant agent i is to forming a preference for category j , the attention u_i represents how attentive agent i is to the preferences of other agents, and the self-reinforcement α_{ij} represents how resistant agent i is to changing its preference about category j .

The parameters a_{jk}^a , a_{jl}^o , and b_{ij} are extrinsic to the agent. The communication matrix $[a_{ik}^a]$ describes the communication strength between agent i and agent k , the belief matrix $[a_{jl}^o]$ describes the correlation of preferences for category j and category l , and the environmental input b_{ij} describes the impact of the environment on an agent's the preference for category j . The saturating function \mathcal{S} is selected so that $S(0) = 0$, $S'(0) = 1$, and $S'''(0) \neq 0$ [23]. We use a hyperbolic tangent for the saturation function in our experiments.

For a given communication matrix $[a_{jl}^o]$ and belief matrix $[a_{jl}^o]$, the sensitivity of preference formation is determined by an agent's intrinsic parameters d_{ij} , u_i , and α_{ij} ; and the equilibrium value of each preference is a function of the environmental input b_{ij} (see Figure 2).

Mutually exclusive categories. In the nonlinear opinion dynamics framework, mutually exclusive categories are negatively correlated. Consider, for example, a system with two categories. The categories are mutually exclusive if $a_{12}^o, a_{21}^o \leq 0$. Since $z_{i1} = -cz_{i2}$, we can decouple the dynamics for z_{i1} and z_{i2} and only model the preference for one category. Equation (1) therefore reduces to

$$\dot{z}_i = -d_i z_i + \mathcal{S} \left(u_i \left(\tilde{\alpha}_i z_i + \sum_{\substack{k=1 \\ k \neq i}}^{\mathcal{N}_a} \tilde{a}_{ik} z_{kj} \right) \right) + b_i. \quad (2)$$

Additional details are provided in Appendix C.1. Mutually exclusive categories provides a systematic way to identify opportunities for dimensionality reduction.

4 Method

In this section we present our BINN model for relational inference (see Figure 3). Given trajectories of a multi-agent system, our goal is to predict agent behavior in an interpretable way by inferring the intrinsic and

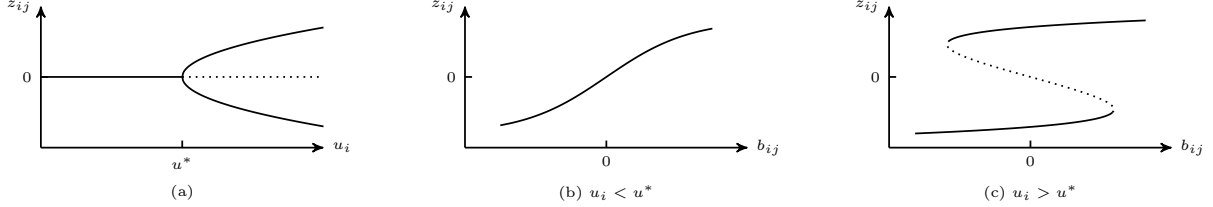


Figure 2: **Sensitivity to environmental inputs b_{ij} .** Solid lines represent stable equilibria and dotted line represents unstable equilibria. (a) We show the pitchfork bifurcation characteristic to equation 1. The number, location, and stability of equilibria changes with the attention parameter u_i . (b) For attention $u_i < u^*$ preferences change linearly with environmental inputs. (c) For attention $u_i > u^*$ preferences change rapidly in response to environmental inputs with hysteresis encoding memory of previous states.

extrinsic characteristics of agents as described by the nonlinear opinion dynamics model (see Section 3).

We define a multi-agent system as a system of $N_a \in \mathbb{N}$ agents, each with real-valued preference for a set of $N_o \in \mathbb{N}$ categories. We learn a mapping between the observed behavior of agents and their preferences for a set of latent categories using a graph neural network; and the parameters of a nonlinear opinion dynamics model which determine the evolution of agent preferences.

We model the evolution of agent preference by the dynamical equation presented in Equation 1. With this formulation, we can control agent preferences by varying the environmental input as shown in Figure 5.

We train our model using N trajectories of T observations, where each observation has dimension d . For a given trajectory, we denote the observed state of agent i at time t by $\mathbf{x}_{i,t} \in \mathbb{R}^d$, and the preferences of agent i at time t by $\mathbf{z}_{i,t} \in \mathbb{R}^{N_o}$.

4.1 Encoder

We use separate encoding networks to learn the mappings from agent states to agent preferences and from agent states to environmental inputs. We refer to the first of these encoders as the preference encoder E_z , and the latter as the environmental input encoder E_b .

Each encoder takes state observations of the multi-agent system at time t as input and processes them in an MPNN [54]. The multi-agent system is represented as a fully-connected graph with node values determined by the physical state of each agent.

Formally, the preference encoder E_z performs the following message passing functions for agent i at timestep t :

$$\mathbf{z}'_{i,t} = f_{\text{emb}}^z(\mathbf{x}_{i,t}), \quad (3)$$

$$v \rightarrow e : \quad \mathbf{m}_{(i,k),t}^z = f_{v \rightarrow e}^z(\mathbf{z}'_{i,t}, \mathbf{z}'_{k,t}), \quad (4)$$

$$e \rightarrow v : \quad \mathbf{z}_{i,t} = f_{e \rightarrow v}^z\left(\sum_{k \neq i} \mathbf{m}_{(i,k),t}^z, \mathbf{z}'_{i,t}\right), \quad (5)$$

where f_{emb}^z , $f_{v \rightarrow e}^z$, and $f_{e \rightarrow v}^z$ are 3-layer MLPs. The environmental input encoder E_b is designed similarly, and performs the following message passing functions for agent i at timestep t :

$$\mathbf{b}'_{i,t} = f_{\text{emb}}^b(\mathbf{x}_{i,t}), \quad (6)$$

$$v \rightarrow e : \quad \mathbf{m}_{(i,k),t}^b = f_{v \rightarrow e}^b(\mathbf{b}'_{i,t}, \mathbf{b}'_{k,t}), \quad (7)$$

$$e \rightarrow v : \quad \mathbf{b}_{i,t} = f_{e \rightarrow v}^b\left(\sum_{k \neq i} \mathbf{m}_{(i,k),t}^b, \mathbf{b}'_{i,t}\right), \quad (8)$$

where f_{emb}^b , $f_{v \rightarrow e}^b$, and $f_{e \rightarrow v}^b$ are 3-layer MLPs.

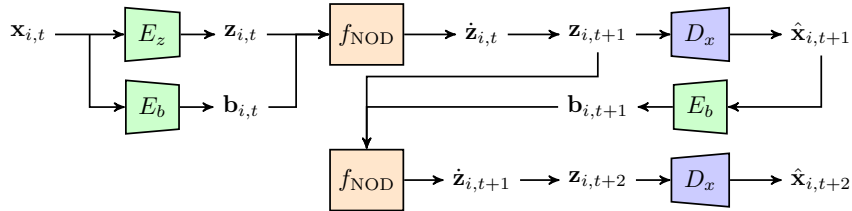


Figure 3: **Behavior-inspired neural network architecture overview.** Our network takes agent states as inputs and outputs predicted next states, while maintaining a representation of agent preferences for a set of latent categories. The network E_z encodes physical states to preferences for a set of latent categories and E_b encodes physical states into latent environmental inputs. In the latent space, we compute future preferences using the nonlinear opinion dynamics block f_{NOD} , and use the decoder D_x to map predicted preferences to predicted physical states. The latent dynamics are unrolled for multi-step trajectory prediction.

4.2 Latent nonlinear opinion dynamics

We use the nonlinear opinion dynamics formulation in Equation (1) to model the evolution of agent preferences on a set of latent categories,

$$\dot{\mathbf{z}}_{i,t+1} = f_{\text{NOD}}(\mathbf{z}_{i,t}, \mathbf{b}_t, \mathbf{A}_t^a). \quad (9)$$

We learn the intrinsic agent parameters, \mathbf{d} , \mathbf{u} , and $\boldsymbol{\alpha}$, the extrinsic parameter \mathbf{A}^o , and compute the inter-agent communication matrix \mathbf{A}_t^a at each timestep t .

We compute future preferences using Euler integration,

$$\mathbf{z}_{i,t+1} = \mathbf{z}_{i,t} + f_{\text{NOD}}(\mathbf{z}_{i,t}, \mathbf{b}_t, \mathbf{A}_t^a) \Delta t, \quad (10)$$

where Δt is dataset dependent.

4.3 Communication matrix

We define the communication matrix \mathbf{A}_t^a as a function of inter-agent proximity. In our baseline BINN model, we define \mathbf{A}_t^a as the distance between observed positions,

$$a_{(i,j),t}^a = \|\mathbf{p}_{i,t} - \mathbf{p}_{j,t}\|^2. \quad (11)$$

We also introduce *Behavior-Inspired Neural Network*+(BINN+), where we incorporate an informed hypothesis of how agents in the system communicate. For example, for systems in which agents have more influence on each other when they are closer (e.g., human interaction) we define \mathbf{A}_t^a as the inverse distance between observed positions,

$$a_{(i,j),t}^a = \frac{1}{\|\mathbf{p}_{i,t} - \mathbf{p}_{j,t}\|^2 + \epsilon} \quad (12)$$

where ϵ is small.

4.4 Decoder

Our decoding network D_x is an MPNN [54] that maps agent preferences to predictions of agent states. At every timestep t , the latent preferences of the multi-agent system are represented as a fully-connected graph with node values determined by the preferences of each agent.

Formally, our decoder D_x performs the following message passing functions for agent i at timestep t :

$$\hat{\mathbf{x}}'_{i,t} = f_{\text{dec}}^x(\mathbf{z}_{i,t}), \quad (13)$$

$$v \rightarrow e : \mathbf{m}_{(i,k),t}^x = f_{v \rightarrow e}^x(\hat{\mathbf{x}}'_{i,t}, \hat{\mathbf{x}}'_{k,t}), \quad (14)$$

$$e \rightarrow v : \hat{\mathbf{x}}_{i,t} = f_{e \rightarrow v}^x \left(\sum_{k \neq i} \mathbf{m}_{(i,k),t}^x, \hat{\mathbf{x}}'_{i,t} \right), \quad (15)$$

where f_{dec}^x , $f_{v \rightarrow e}^x$, and $f_{e \rightarrow v}^x$ are 3-layer MLPs.

4.5 Loss function

We train our model using the three component loss function,

$$\mathcal{L} = \mathcal{L}_{\text{pred}} + \gamma_1 \mathcal{L}_{\text{recon}} + \gamma_2 \mathcal{L}_{\text{latent}} \quad (16)$$

where $\mathcal{L}_{\text{pred}}$ is the prediction loss, $\mathcal{L}_{\text{recon}}$ is the reconstruction loss and $\mathcal{L}_{\text{latent}}$ is the latent loss.

The prediction loss, $\mathcal{L}_{\text{pred}}$, is defined as the dissimilarity between the ground truth future state $\mathbf{x}_{i,t}$, and the predicted future state $\hat{\mathbf{x}}_{i,t}$,

$$\mathcal{L}_{\text{pred}} = \frac{1}{T\mathcal{N}_a} \sum_{t=1}^T \sum_{i=1}^{\mathcal{N}_a} \left\| \mathbf{x}_{i,t} - \hat{\mathbf{x}}_{i,t} \right\|^2, \quad (17)$$

and encourages accuracy of future state prediction. The reconstruction loss, $\mathcal{L}_{\text{recon}}$, is defined as the dissimilarity between the ground truth initial state $\mathbf{x}_{i,0}$, and the reconstructed initial state,

$$\mathcal{L}_{\text{recon}} = \frac{1}{\mathcal{N}_a} \sum_{i=1}^{\mathcal{N}_a} \left\| \mathbf{x}_{i,0} - (D_x \circ E_z)(\mathbf{x}_{i,0}) \right\|^2, \quad (18)$$

and encourages the decoder to function as the inverse of the encoder. The latent loss, $\mathcal{L}_{\text{latent}}$, is defined as the dissimilarity of preferences predicted by the dynamical model and those encoded by the preference encoder,

$$\mathcal{L}_{\text{latent}} = \frac{1}{T\mathcal{N}_a} \sum_{t=1}^T \sum_{i=1}^{\mathcal{N}_a} \left\| \mathbf{z}_{i,t+1} - f_{\text{NOD}}(\mathbf{z}_{i,t}) \right\|^2, \quad (19)$$

and encourages alignment between the representations encoded by E_z and those predicted by f_{NOD} .

5 Experiments

In this section, we highlight the utility of our model for discovering interpretable representations useful for dimensionality reduction, and its efficacy for long-horizon trajectory prediction. Dataset and training details are provided in Appendices A and B.

5.1 Interpretability of the latent space

We demonstrate the interpretability of our latent representations on both the pendulum and double pendulum datasets.

Pendulum. We model the pendulum as a single agent system represented as a graph with a single node. We construct a graphical representation at every timestep and set the node feature to the concatenation of the position and velocity of the pendulum bob.

The relationship between observed physical states and learned preferences is shown in Figure 4. Our model

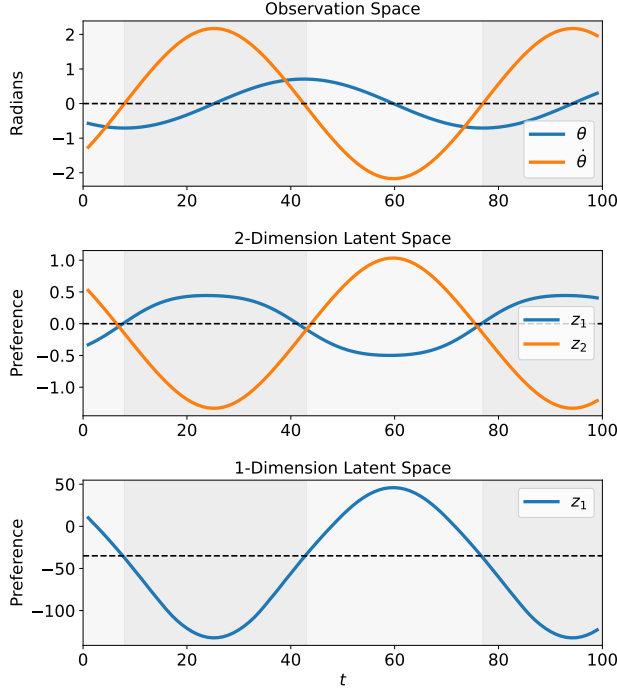


Figure 4: **Mutually exclusive pendulum preferences.** We show the observed, and latent representations of the pendulum bob. **(Top-bottom)** The observed position and velocity of the pendulum bob; the learned representation of agent preferences on a 2-dimensional latent space, and the learned representation of agent preferences on a 1-dimensional latent space. In the 2-dimensional space, preferences are perfectly out of phase indicating that they are mutually exclusive.

suggest the pendulum is a 1-dimensional system which is consistent with physical understanding. We can see this in two ways. First, since preferences z_1 and z_2 switch signs when the pendulum bob changes direction, we can interpret the learned categories as a desire to move clockwise ($z_1 > 0$) and a desire to move counter-clockwise ($z_2 > 0$). Moreover, the two preferences are perfectly out-of-phase and therefore mutually exclusive. This observation is supported by consideration of the learned belief matrix whose entries satisfy the condition for mutual exclusivity, i.e., $a_{12}^o, a_{21}^o \leq 0$,

$$\mathbf{A}^o = \begin{bmatrix} 0 & -1.2947 \\ -0.9147 & 0 \end{bmatrix}. \quad (20)$$

The conditions for mutual exclusivity are described in Section 3.1.

We empirically verify that the dynamics of this system can be captured with a 1-dimensional latent space. The prediction error for models with a 2-dimensional and 1-dimensional latent space are comparable i.e., $1.9718\text{e-}3$ MSE and $1.9916\text{e-}3$ MSE respectively. Qualitative

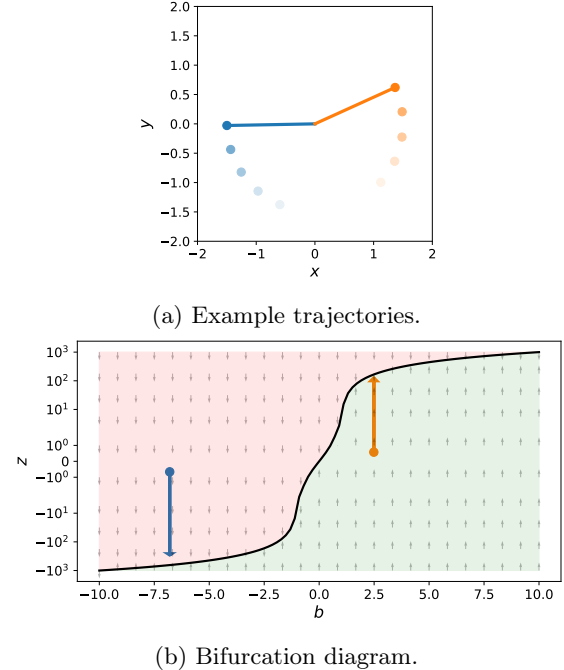


Figure 5: **Pendulum preference bifurcation diagram.** **(a)** We show a pendulum trajectory with clockwise motion (blue) and counterclockwise motion (orange). **(b)** The initial preferences are near neutral, but large environmental inputs drive preferences in opposite directions resulting in opposite motions in the physical space.

results are shown in Figure 4 (bottom).

In addition to providing a mechanism for identifying opportunities for dimensionality reduction, the nonlinear opinion dynamics inductive bias also provides a mechanism for controlling preference formation through the environmental input b_{ij} . We show trajectories with different rotational directions in Figure 5a, and their corresponding environmental input latent preference pairs, (b_{ij}, z_{ij}) , on the bifurcation diagram in Figure 5b. The initial preferences for both trajectories are near neutral, but the initial environmental inputs are far from zero. The negative environmental input drives the initial preference of the blue trajectory toward an equilibrium in the preference space that corresponds to a strongly negative preference, and a clockwise motion in the physical space. The positive environmental input drives the initial preference of the orange trajectory toward an equilibrium in the preference space that corresponds to a strongly positive preference, and a counterclockwise motion in the physical space.

Double pendulum. We use the double pendulum dataset to demonstrate interpretability in a more complex setting. We model the double pendulum as a two agent system represented as a graph with a two

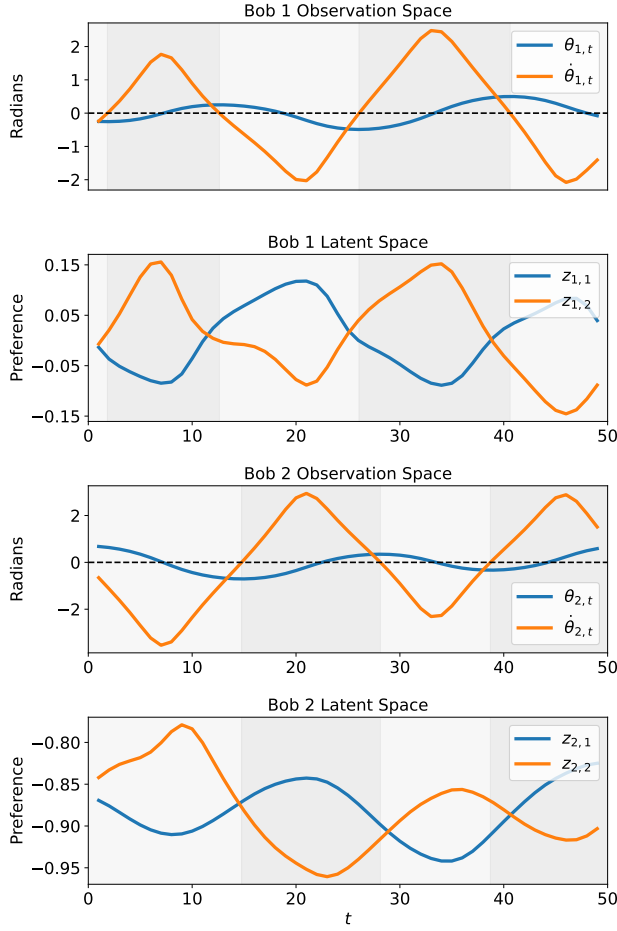


Figure 6: **Non-mutually exclusive double pendulum preferences.** We show the observed, and latent representations of each double pendulum bob. **(Top-bottom)** The observed position and velocity of the first bob; the learned preferences of the first bob; the observed position and velocity of the second bob; the learned preferences of the second bob. When preference switch, physical bob’s motion switches direction.

nodes. We construct a graphical representation at every timestep and set node features to the concatenation of the position and velocity of the corresponding double pendulum bob.

The relationship between the observed physical states and the learned preferences is shown in Figure 6. For the first bob, when the preference $z_{1,1}$ switches from greater (less) than to less (greater) than preference $z_{1,2}$, the physical bob switches from clockwise (counterclockwise) to counterclockwise (clockwise) motion. The opposite is true for the second bob. This behavior is observed across examples (see Appendix C.2). In contrast to pendulum preferences, double pendulum preferences are non-mutually exclusive. This observation is supported by the belief matrix, which does not satisfy the mutually-exclusive condition described in

Table 1: **Trajectory prediction.** Trajectory prediction error on the Mass-Spring, Kuramoto, and TrajNet++ datasets is reported. Our BNN and BNN+ models outperform baseline models on all datasets.

Network	Mass-Spring	Kuramoto	TrajNet++
BINN*	2.88×10^{-4}	4.52×10^{-3}	2.16×10^{-2}
BINN+*	2.88×10^{-4}	4.52×10^{-3}	1.20×10^{-2}
NRI [19]	3.73×10^{-3}	8.20×10^{-3}	8.49×10^{-2}
dNRI [20]	4.86×10^{-3}	6.41×10^{-3}	4.00×10^{-2}

Section 3.1,

$$\mathbf{A}^o = \begin{bmatrix} 0 & -2.8137 \\ 1.1597 & 0 \end{bmatrix}. \quad (21)$$

5.2 Trajectory prediction

We demonstrate the efficacy of our model for trajectory prediction on several datasets. We report the quantitative performance of our model against competitive baselines in Table 1, and show the qualitative performance of our model in Figure 7. Dataset details are provided in Appendix A.

5.2.1 Mechanical systems

Mass-spring. We demonstrate the utility of our model for trajectory prediction on the mass-spring dataset. The system consists of five masses and the dynamics are governed by a second-order linear equation. To model this system, we construct a fully-connected graph with five nodes and initialize node features as the concatenation of the position and velocity of the individual masses.

For both the BNN and BNN+ models we compute the communication matrix using the inter-agent distance defined in Equation (11). Our BNN models outperform both the NRI [19] and dNRI [20] models by an order of magnitude.

Kuramoto oscillator. The Kuramoto oscillator dataset describes a 5-agent system with dynamics governed by a first-order nonlinear equation. To model this system, we construct a fully-connected graph with five nodes and initialize node features with the vector formed by concatenating the position and velocity of each oscillator.

For both the BNN and BNN+ models we compute the communication matrix using the inter-agent distance defined in Equation (11). On this dataset, our BNN models perform comparably with baseline models.

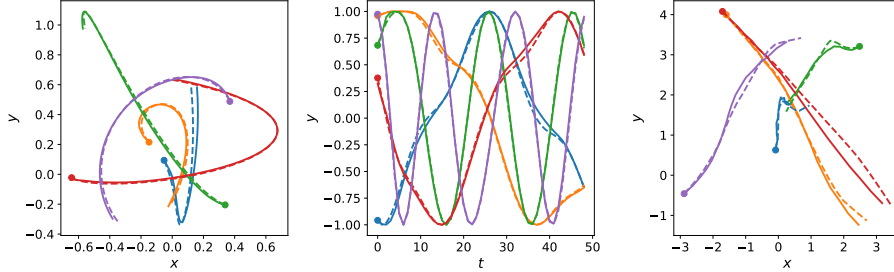


Figure 7: **Trajectory prediction.** We show trajectories predicted by BNN (solid) and the corresponding ground truths (dashed). (Left-right) Examples from mass-spring, Kuramota oscillator, and TrajNet++ datasets.

5.2.2 Pedestrian behavior

TrajNet++ simulator. We evaluate our model on a synthetic subset of the TrajNet++ [55, 56] dataset where each trajectory contains 5 agents.

For our BNN model, we compute the communication matrix using the inter-agent distance as defined in Equation (11). For our BNN+ model, however, we assume pedestrian sensing scales inversely with inter-agent distance and introduce a prior $\tilde{\mathbf{A}}_{(i,j),t}^a$ on the communication matrix,

$$\tilde{\mathbf{A}}_{(i,j),t}^a = \frac{1}{\|\mathbf{p}_{i,t} - \mathbf{p}_{j,t}\|^2 + \epsilon}, \quad (22)$$

where ϵ is very small. We augment $\tilde{\mathbf{A}}_{(i,j),t}^a$ with a learned multiplier $\mathbf{A}_{(i,j)}^{\text{pre}}$ which together determine the communication matrix,

$$\mathbf{A}_{(i,j),t}^a = \mathbf{A}_{(i,j)}^{\text{pre}} \odot \tilde{\mathbf{A}}_{(i,j),t}^a. \quad (23)$$

On this dataset, our BNN and BNN+ models outperform competitive baselines.

The relationship between the observed trajectories and learned preferences is shown in Figure 8. Three consistent trends emerge across examples. First, when the relative magnitudes of z_{i1} and z_{i1} change, the direction of travel changes from right to left. Second, when the relative magnitude of z_{i3} to z_{i4} increases, agents increase their y-velocity. Finally, the dominant z_{i3} in row 1 and 2 results in downwards motion, while the dominant z_{i4} in row 3 results in upwards motion.

6 Conclusion

In this paper we address the challenge of designing a relational inference model with inter-agent relationships that are informed by preferences for multiple categories. To do this, we propose the use of nonlinear opinion dynamics as an inductive bias, and introduce an interpretable and flexible relational inference model. In addition to outperforming competitive existing relational inference models on multiple trajectory prediction datasets, our model provides a mechanisms

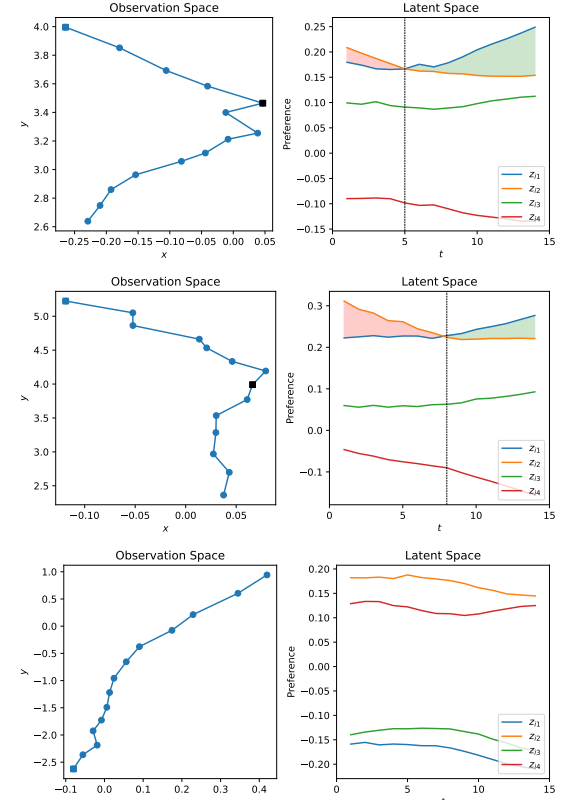


Figure 8: **TrajNet++ preferences.** (Left) We visualize example trajectories from the dataset. The initial position of the trajectory is marked by a blue square and the point of direction change is marked by a black square. (Right) We plot agent preferences for each latent categories. Dominant z_{i1} corresponds to leftwards motion and dominant z_{i2} corresponds to rightward motion. Dominant z_{i3} corresponds to downwards motion and dominant z_{i4} corresponds to upwards motion.

for identification of mutually exclusive categories, and controlling preference formation.

Limitations and future work. Similarly to prior work, our BNN models assume the same agents are present throughout a trajectory. Efforts to address this limitation would broaden the applicability of this work.

References

[1] Pablo Villanueva-Domingo, Francisco Villaescusa-Navarro, Daniel Anglés-Alcázar, Shy Genel, Federico Marinacci, David N Spergel, Lars Hernquist, Mark Vogelsberger, Romeel Dave, and Desika Narayanan. Inferring halo masses with graph neural networks. *The Astrophysical Journal*, 935(1):30, 2022.

[2] Pablo Lemos, Niall Jeffrey, Miles Cranmer, Shirley Ho, and Peter Battaglia. Rediscovering orbital mechanics with machine learning. *Machine Learning: Science and Technology*, 4(4):045002, 2023.

[3] Edward Fiorelli, Naomi Ehrich Leonard, Pradeep Bhatta, Derek A Paley, Ralf Bachmayer, and David M Fratantoni. Multi-auv control and adaptive sampling in monterey bay. *IEEE journal of oceanic engineering*, 31(4):935–948, 2006.

[4] George F Young, Luca Scardovi, Andrea Cavagna, Irene Giardina, and Naomi E Leonard. Starling flock networks manage uncertainty in consensus at low cost. *PLoS computational biology*, 9(1):e1002894, 2013.

[5] Thomas D. Seeley, P. Kirk Visscher, Thomas Schlegel, Patrick M. Hogan, Nigel R. Franks, and James A. R. Marshall. Stop signals provide cross inhibition in collective decision-making by honeybee swarms. *Science*, 335(6064):108–111, 2012.

[6] Emanuel Gull, Olivier Parcollet, and Andrew J Millis. Superconductivity and the pseudogap in the two-dimensional hubbard model. *Physical review letters*, 110(21):216405, 2013.

[7] Antoine Browaeys and Thierry Lahaye. Many-body physics with individually controlled rydberg atoms. *Nature Physics*, 16(2):132–142, 2020.

[8] Zhe Wang, Petar Veličković, Daniel Hennes, Nenad Tomašev, Laurel Prince, Michael Kaisers, Yoram Bachrach, Romuald Elie, Li Kevin Wenliang, Federico Piccinini, et al. Tacticai: an ai assistant for football tactics. *Nature communications*, 15(1):1–13, 2024.

[9] Sandro Hauri, Nemanja Djuric, Vladan Radosavljevic, and Slobodan Vucetic. Multi-modal trajectory prediction of nba players. In *Proceedings of the IEEE/CVF Winter Conference on Applications of Computer Vision*, pages 1640–1649, 2021.

[10] Sepp Hochreiter and Jürgen Schmidhuber. Long short-term memory. *Neural computation*, 9(8):1735–1780, 1997.

[11] Ilya Sutskever, Oriol Vinyals, and Quoc V Le. Sequence to sequence learning with neural networks. *Advances in neural information processing systems*, 27, 2014.

[12] Alexandre Alahi, Kratarth Goel, Vignesh Ramathan, Alexandre Robicquet, Li Fei-Fei, and Silvio Savarese. Social lstm: Human trajectory prediction in crowded spaces. In *Proceedings of the IEEE conference on computer vision and pattern recognition*, pages 961–971, 2016.

[13] Agrim Gupta, Justin Johnson, Li Fei-Fei, Silvio Savarese, and Alexandre Alahi. Social gan: Socially acceptable trajectories with generative adversarial networks. In *Proceedings of the IEEE conference on computer vision and pattern recognition*, pages 2255–2264, 2018.

[14] Sergio Casas, Wenjie Luo, and Raquel Urtasun. Intentnet: Learning to predict intention from raw sensor data. In *Conference on Robot Learning*, pages 947–956. PMLR, 2018.

[15] Nachiket Deo and Mohan M Trivedi. Convolutional social pooling for vehicle trajectory prediction. In *Proceedings of the IEEE conference on computer vision and pattern recognition workshops*, pages 1468–1476, 2018.

[16] Amir Sadeghian, Vineet Kosaraju, Ali Sadeghian, Noriaki Hirose, Hamid Rezatofighi, and Silvio Savarese. Sophie: An attentive gan for predicting paths compliant to social and physical constraints. In *Proceedings of the IEEE/CVF conference on computer vision and pattern recognition*, pages 1349–1358, 2019.

[17] Sainbayar Sukhbaatar, Rob Fergus, et al. Learning multiagent communication with backpropagation. *Advances in neural information processing systems*, 29, 2016.

[18] Adam Santoro, David Raposo, David G Barrett, Mateusz Malinowski, Razvan Pascanu, Peter Battaglia, and Timothy Lillicrap. A simple neural network module for relational reasoning. *Advances in neural information processing systems*, 30, 2017.

[19] Thomas Kipf, Ethan Fetaya, Kuan-Chieh Wang, Max Welling, and Richard Zemel. Neural relational inference for interacting systems. In *International conference on machine learning*, pages 2688–2697. PMLR, 2018.

[20] Colin Graber and Alexander G Schwing. Dynamic neural relational inference. In *Proceedings of the IEEE/CVF Conference on Computer Vision and Pattern Recognition*, pages 8513–8522, 2020.

[21] Chenxin Xu, Maosen Li, Zhenyang Ni, Ya Zhang, and Siheng Chen. Groupnet: Multiscale hypergraph neural networks for trajectory prediction with relational reasoning. In *Proceedings of the IEEE/CVF Conference on Computer Vision and Pattern Recognition*, pages 6498–6507, 2022.

[22] Chenxin Xu, Robby T Tan, Yuhong Tan, Siheng Chen, Yu Guang Wang, Xinchao Wang, and Yanfeng Wang. Eqmotion: Equivariant multi-agent motion prediction with invariant interaction reasoning. In *Proceedings of the IEEE/CVF Conference on Computer Vision and Pattern Recognition*, pages 1410–1420, 2023.

[23] Naomi Ehrich Leonard, Anastasia Bizyaeva, and Alessio Franci. Fast and flexible multiagent decision-making. *Annual Review of Control, Robotics, and Autonomous Systems*, 7, 2024.

[24] Naomi Ehrich Leonard, Keena Lipsitz, Anastasia Bizyaeva, Alessio Franci, and Yphtach Lelkes. The nonlinear feedback dynamics of asymmetric political polarization. *Proceedings of the National Academy of Sciences*, 118(50):e2102149118, 2021.

[25] Alessio Franci, Anastasia Bizyaeva, Shinkyu Park, and Naomi Ehrich Leonard. Analysis and control of agreement and disagreement opinion cascades. *Swarm Intelligence*, 15(1):47–82, 2021.

[26] Wilbert Samuel Rossi and Paolo Frasca. Opinion dynamics with topological gossiping: Asynchronous updates under limited attention. *IEEE Control Systems Letters*, 4(3):566–571, 2020.

[27] Abhimanyu Das, Sreenivas Gollapudi, and Kamesh Munagala. Modeling opinion dynamics in social networks. In *Proceedings of the 7th ACM international conference on Web search and data mining*, pages 403–412, 2014.

[28] Haimin Hu, Kensuke Nakamura, Kai-Chieh Hsu, Naomi Ehrich Leonard, and Jaime Fernández Fisac. Emergent coordination through game-induced nonlinear opinion dynamics. In *2023 62nd IEEE Conference on Decision and Control (CDC)*, 2023.

[29] Charlotte Cathcart, María Santos, Shinkyu Park, and Naomi Ehrich Leonard. Opinion-driven robot navigation: Human-robot corridor passing. 2022.

[30] Anastasia Bizyaeva, Giovanna Amorim, María Santos, Alessio Franci, and Naomi Ehrich Leonard. Switching transformations for decentralized control of opinion patterns in signed networks: Application to dynamic task allocation. *IEEE Control Systems Letters*, 6:3463–3468, 2022.

[31] Giovanna Amorim, María Santos, Shinkyu Park, Alessio Franci, and Naomi Ehrich Leonard. Threshold decision-making dynamics adaptive to physical constraints and changing environment. *arXiv preprint arXiv:2312.06395*, 2023.

[32] Steven L Brunton, Joshua L Proctor, and J Nathan Kutz. Discovering governing equations from data by sparse identification of nonlinear dynamical systems. *Proceedings of the national academy of sciences*, 113(15):3932–3937, 2016.

[33] Nicholas Galioto and Alex Arkady Gorodetsky. Bayesian system id: optimal management of parameter, model, and measurement uncertainty. *Nonlinear Dynamics*, 102(1):241–267, 2020.

[34] Juan A Paredes, Yulong Yang, and Dennis S Bernstein. Output-only identification of self-excited systems using discrete-time lur'e models with application to a gas-turbine combustor. *International Journal of Control*, 97(2):187–212, 2024.

[35] Riley J Richards, Yulong Yang, Juan A Paredes, and Dennis S Bernstein. Output-only identification of lur'e systems with hysteretic feedback nonlinearities. In *2024 American Control Conference (ACC)*, pages 2891–2896. IEEE, 2024.

[36] Karttikeya Mangalam, Harshayu Girase, Shreyas Agarwal, Kuan-Hui Lee, Ehsan Adeli, Jitendra Malik, and Adrien Gaidon. It is not the journey but the destination: Endpoint conditioned trajectory prediction. In *Computer Vision–ECCV 2020: 16th European Conference, Glasgow, UK, August 23–28, 2020, Proceedings, Part II 16*, 2020.

[37] Anirudh Vemula, Katharina Muelling, and Jean Oh. Social attention: Modeling attention in human crowds. In *2018 IEEE international Conference on Robotics and Automation (ICRA)*, pages 4601–4607. IEEE, 2018.

[38] Ye Yuan, Xinshuo Weng, Yanglan Ou, and Kris M Kitani. Agentformer: Agent-aware transformers for socio-temporal multi-agent forecasting. In *Proceedings of the IEEE/CVF International Conference on Computer Vision*, pages 9813–9823, 2021.

[39] Francesco Giuliani, Irtiza Hasan, Marco Cristani, and Fabio Galasso. Transformer networks for trajectory forecasting. In *2020 25th international conference on pattern recognition (ICPR)*, pages 10335–10342. IEEE, 2021.

[40] Cunjun Yu, Xiao Ma, Jiawei Ren, Haiyu Zhao, and Shuai Yi. Spatio-temporal graph transformer networks for pedestrian trajectory prediction. In *Computer Vision–ECCV 2020: 16th European*

Conference, Glasgow, UK, August 23–28, 2020, *Proceedings, Part XII 16*, pages 507–523. Springer, 2020.

[41] Jiyang Gao, Chen Sun, Hang Zhao, Yi Shen, Dragomir Anguelov, Congcong Li, and Cordelia Schmid. Vectornet: Encoding hd maps and agent dynamics from vectorized representation. In *Proceedings of the IEEE/CVF Conference on Computer Vision and Pattern Recognition*, pages 11525–11533, 2020.

[42] Francesco Bullo. *Lectures on network systems*, volume 1. CreateSpace, 2018.

[43] Herbert Levine, Wouter-Jan Rappel, and Inon Cohen. Self-organization in systems of self-propelled particles. *Physical Review E*, 63(1):017101, 2000.

[44] Naomi E Leonard, Derek A Paley, Russ E Davis, David M Fratantoni, Francois Lekien, and Fumin Zhang. Coordinated control of an underwater glider fleet in an adaptive ocean sampling field experiment in monterey bay. *Journal of Field Robotics*, 27(6):718–740, 2010.

[45] Eric W Justh and PS Krishnaprasad. Natural frames and interacting particles in three dimensions. In *Proceedings of the 44th IEEE Conference on Decision and Control*, pages 2841–2846. IEEE, 2005.

[46] Naomi Ehrich Leonard, Derek A Paley, Francois Lekien, Rodolphe Sepulchre, David M Fratantoni, and Russ E Davis. Collective motion, sensor networks, and ocean sampling. *Proceedings of the IEEE*, 95(1):48–74, 2007.

[47] Michele Ballerini, Nicola Cabibbo, Raphael Candelier, Andrea Cavagna, Evaristo Cisbani, Irene Giardina, Vivien Lecomte, Alberto Orlandi, Giorgio Parisi, Andrea Procaccini, et al. Interaction ruling animal collective behavior depends on topological rather than metric distance: Evidence from a field study. *Proceedings of the national academy of sciences*, 105(4):1232–1237, 2008.

[48] Claudio Altafini. Consensus problems on networks with antagonistic interactions. *IEEE transactions on automatic control*, 58(4):935–946, 2012.

[49] Pranav Dandekar, Ashish Goel, and David T Lee. Biased assimilation, homophily, and the dynamics of polarization. *Proceedings of the National Academy of Sciences*, 110(15):5791–5796, 2013.

[50] Martin Golubitsky, Ian Stewart, and David G Schaeffer. *Singularities and Groups in Bifurcation Theory: Volume II*, volume 69. Springer Science & Business Media, 2012.

[51] John Guckenheimer and Philip Holmes. *Nonlinear oscillations, dynamical systems, and bifurcations of vector fields*, volume 42. Springer Science & Business Media, 2013.

[52] Steven H Strogatz. *Nonlinear dynamics and chaos: with applications to physics, biology, chemistry, and engineering*. CRC press, 2018.

[53] Anastasia Bizyaeva, Alessio Franci, and Naomi Ehrich Leonard. Nonlinear opinion dynamics with tunable sensitivity. *IEEE Transactions on Automatic Control*, 68(3):1415–1430, 2022.

[54] Justin Gilmer, Samuel S Schoenholz, Patrick F Riley, Oriol Vinyals, and George E Dahl. Neural message passing for quantum chemistry. In *International conference on machine learning*, pages 1263–1272. PMLR, 2017.

[55] EPFL. Trajnet++ (a trajectory forecasting challenge), 2020.

[56] Parth Kothari, Sven Kreiss, and Alexandre Alahi. Human trajectory forecasting in crowds: A deep learning perspective. *IEEE Transactions on Intelligent Transportation Systems*, 23(7):7386–7400, 2021.

[57] Double pendulum. <https://scienceworld.wolfram.com/physics/DoublePendulum.html>. Accessed: 2024-05-23.

[58] Nvidia. System management interface smi, 2024.

[59] Stacey Peterson. Definition, mebibyte (mib), 2024.

[60] Diederik P. Kingma and Jimmy Ba. Adam: A method for stochastic optimization. In *3rd International Conference on Learning Representations, ICLR*, 2015.

Appendix

A Datasets

In this section we provide data simulation and post processing steps for the dataset used in Section 5. Trajectories are simulated forward in time with a numerical integrator for a certain timestep and length, all given in Table 3. To reduce the dimensionality of the training data while preserving the dynamics of the system, the simulated trajectories are coarsen according the the frequency given in Table 4 to generate the final training data. We note that since Δt is passed into RROD as a fixed hyperparameter for training, the timestep of 1.0 is arbitrarily chosen for TrajNet++.

A.1 Pendulum

We generate a synthetic dataset of pendulum motion where pendulum dynamics are defined by the second order equation,

$$\ddot{\theta} = -\frac{g}{\ell} \sin \theta, \quad (24)$$

with $\ell = 1.0$, $g = 9.81$, and initial conditions sampled from the uniform distribution, $\theta_0, \dot{\theta}_0 \sim \mathcal{U}(-0.5\pi, 0.5\pi)$. The dataset consists of 50000 training trajectories, and 12500 validation and testing trajectories, simulated subject to parameters given in Table 3.

A.2 Double pendulum

We generate a synthetic dataset of double pendulum motion where double pendulum dynamics are defined by the second order equations in [57]. The pendulum arms are defined $\ell_1 = \ell_2 = 1.0$, pendulum bobs are defined $m_1 = m_2 = 1.0$, gravity is defined $g = 9.81$ and the initial conditions are sampled from the normal distribution, i.e., $\theta_{1,0}, \dot{\theta}_{1,0}, \theta_{2,0}, \dot{\theta}_{2,0} \sim \mathcal{N}(0, 0.5)$. The dataset consists of 50000 training trajectories, and 12500 validation and testing trajectories, simulated subject to parameters given in Table 3.

A.3 Mass-spring

We generate a synthetic dataset of mass spring motion where the mass spring dynamics are defined by the second order linear equation,

$$\ddot{\mathbf{r}}_i = \sum_{j \neq i}^{N_a} -k_{ij} (\mathbf{r}_i - \mathbf{r}_j), \quad (25)$$

where the spring constant k_{ij} is either 2.5 or 0, and $k_{ij} = k_{ji}$. The initial conditions are sampled from the normal distribution, $\mathbf{r}_{i,0}, \dot{\mathbf{r}}_{i,0} \sim \mathcal{N}(0, 0.3)$. The dataset consists of 50000 training trajectories, and 12500 validation and testing trajectories, simulated subject to parameters given in Table 3.

A.4 Kuramoto oscillator

We generate a synthetic dataset of Kuramoto oscillator motion where the oscillator dynamics are defined by the first-order nonlinear equation,

$$\dot{\phi}_i = \omega_i + \sum_{j \neq i} k_{ij} \sin(\phi_i - \phi_j), \quad (26)$$

where the coupling constant k_{ij} is either 2.5 or 0 and $k_{ij} = k_{ji}$. The initial conditions are sampled from the uniform distribution, $\phi_{i,t=0} \sim \mathcal{U}(0, 2\pi)$. The dataset consists of 50000 training trajectories, and 12500 validation and testing trajectories, simulated subject to parameters given in Table 3.

B Training Details

In this section we provide training details on the experiments presented.

All models were trained on Dell Precision 7920 work stations. Each work station contains an Intel Xeon Gold 5220R 24 core CPU, two Nvidia A6000 GPUs, and 256GB of RAM. At training time only 1-GPU is used and the CPU and RAM is shared between two workloads. The hyperparameters used for training is given in Table 4. Furthermore the required memory for training both BINN and baseline models are given in Table 2. The reported values are taken from NVIDIA-smi [58] at the end of the first training epoch, which reports memory usage in terms of mebibyte (MiB) [59]. 1 mebibyte corresponds to 1.04858 megabyte.

Table 2: Memory requirement for RROD, NRI, and dNRI for experiments reported.

Network	Mass-Spring	Kuramoto	TrajNet++
BINN*	496 MiB	484 MiB	406 MiB
NRI	1670 MiB	1658 MiB	916 MiB
dNRI	5008 MiB	4996 MiB	2180 MiB

C Additional Experimental Results

C.1 Separability of Mutually Exclusive Categories

Consider nonlinear opinion dynamics given in Equation (1). Given the assumption that $z_{i1} = -cz_{i2}$, we can reduce terms such that belief term

$$\sum_{l=1, l \neq j}^{N_o} a_{jl}^o z_{il} = a_{21} z_{i2} = -ca_{12} z_{i1}. \quad (27)$$

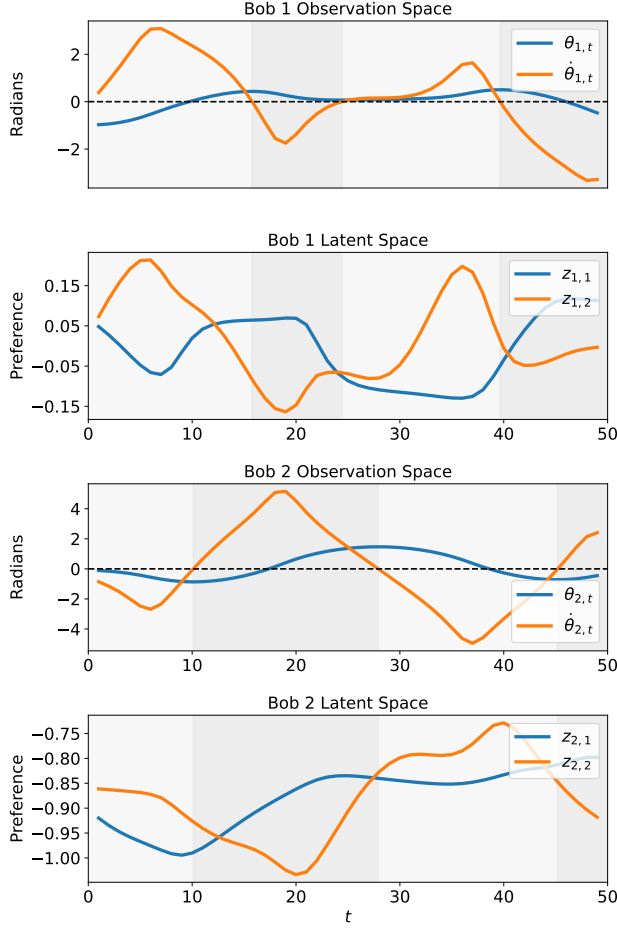


Figure 9: Latent preferences for the double pendulum dataset.

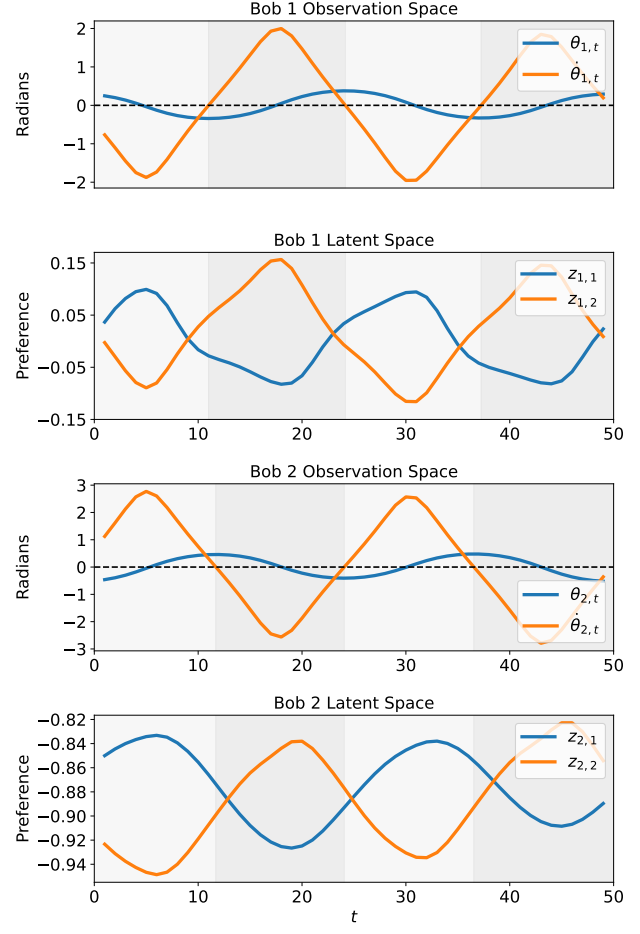


Figure 10: Latent preferences for the double pendulum dataset.

The communication-belief term

$$\sum_{k=1}^{\mathcal{N}_a} \sum_{\substack{l=1 \\ k \neq i}}^{\mathcal{N}_o} a_{ik}^a a_{jl}^o z_{kl} = \sum_{\substack{k=1 \\ k \neq i}}^{\mathcal{N}_a} a_{ik}^a d_{21}^o z_{k2}, \quad (28)$$

$$= \sum_{\substack{k=1 \\ k \neq i}}^{\mathcal{N}_a} -a_{ik}^a c a_{12}^o z_{k1}. \quad (29)$$

And therefore Equation (1) can be decoupled into Equation (2), such that

$$\dot{z}_i = -d_i z_i + \mathcal{S} \left(u_i \left(\tilde{\alpha}_i z_i + \sum_{\substack{k=1 \\ k \neq i}}^{\mathcal{N}_a} \tilde{a}_{ik} z_k \right) \right) + b_i, \quad (30)$$

where

$$\tilde{\alpha}_i = \alpha_{i1} - c a_{12}^o, \quad (31)$$

$$\tilde{a}_{ik} = a_{i1}^a - c a_{i1}^a a_{12}^o. \quad (32)$$

C.2 Double Pendulum

We include additional observation space to preference encoding in Figure 9 and 10.

Table 3: Data generation and post processing parameters for experiments.

	Pendulum	Double Pendulum	Mass-Spring	Kuramoto	TrajNet++
Integrator	RK4	RK4	RK4	RK4	n/a
Δt	1e-3	5e-4	5e-4	5e-4	1.0
Steps	5000	5000	5000	500	n/a
Coarsening	100	100	100	10	n/a

Table 4: Hyperparameter for the experiments.

Hyper-parameter	Pendulum	Double Pendulum	Mass-Spring	Kuramoto	TrajNet++
\mathcal{N}_a	1	2	5	5	5
\mathcal{N}_o	2	2	4	4	4
Epoch	500	500	1000	1000	1000
Batch Size	256	256	256	256	256
Activation	ReLU	ELU	tanh	tanh	tanh
Optimizer	Adam [60]	Adam	Adam	Adam	Adam
Initial Learning Rate	1e-3	1e-3	1e-3	1e-3	5e-4
Hidden Dimension	64	64	128	128	128
Scheduler	N/A	N/A	StepLR	StepLR	StepLR
Scheduler Step	N/A	N/A	200	200	200
Scheduler Gamma	N/A	N/A	0.25	0.25	0.25
γ_1	1.0	1.0	1.0	1.0	1.0
γ_2	1.0	1.0	1.0	1.0	1.0